Flame front tracking in turbulent lean premixed flames using stereo PIV and time-sequenced planar LIF of OH

G. Hartung · J. Hult · R. Balachandran · M.R. Mackley · C.F. Kaminski

Abstract This paper describes the simultaneous application of time-sequenced laser-induced fluorescence imaging of OH radicals and stereoscopic particle image velocimetry for measurements of the flame front dynamics in lean and premixed LP turbulent flames. The studied flames could be acoustically driven, to simulate phenomena important in LP combustion technologies. In combination with novel image post processing techniques we show how the data obtained can be used to track the flame front contour in a plane defined by the illuminating laser sheets. We consider effects of chemistry and convective fluid motion on the dynamics of the observed displacements and analyse the influence of turbulence and acoustic forcing on the observed contour velocity, a quantity we term as s_d^{2D}. We show that this quantity is a valuable and sensitive indicator of flame turbulence interactions, as (a) it is measurable with existing experimental methodologies, and (b) because computational data, e.g. from large eddy simulations, can be post processed in an identical fashion. s_d^{2D} is related (to a two-dimensional projection) of the three-dimensional flame displacement speed s_d, but artifacts due to out of plane convective motion of the flame surface and the uncertainty in the angle of the flame surface normal have to be carefully considered. Monte Carlo simulations were performed to estimate such effects for several distributions of flame front angle distributions, and it is shown conclusively that s_d^{2D} is a sensitive indicator of a quantity related to s_d in the flames we study. s_d^{2D} was shown to increase linearly both with turbulent intensity and with the amplitude of acousting forcing for the range of conditions studied.

PACS 01.30.-y

1 Introduction

Turbulent lean premixed (LP) combustion is of high interest in many industrial applications offering reduced levels of pollutant emissions, such as CO, soot and NO as well as improving fuel efficiency. Over recent years large efforts have been made to explore fundamental correlations of LP flame properties for model testing and to improve predictive capabilities. Laser-based techniques in laboratory scale combustors are crucial in this effort as they enable high-quality measurements of turbulent flame properties, such as local curvature, heat release, turbulent burning velocity, instantaneous stretch, and the concentration of important chemical species under well controlled conditions. Among these flame properties, the local turbulent burning velocity, which is normal to the surface of the wrinkled flamefront, is among the most important. Turbulent burning velocity statistics are important for the modelling of the level set equation in direct numerical simulations (DNS), in Reynolds averaged Navier–Stokes approaches and for large eddy simulations (LES), where local effects have to be included into sub-grid scale (SGS) models [1].

G. Hartung · J. Hult · M.R. Mackley · C.F. Kaminski (✉)
University of Cambridge, Department of Chemical Engineering,
Pembroke Street, Cambridge, CB2 3RA, UK
e-mail: cfk23@cam.ac.uk

R. Balachandran
University College London, Department of Mechanical
Engineering, Torrington Place, London, WC1E 7JE, UK

C.F. Kaminski
SAOT School of Advanced Optical Technologies, Max Planck
Institute for the Science of Light, Division III, University of
Erlangen-Nuremberg, Günther-Scharowsky-Str. 1, 91058
Erlangen, Germany

In the literature two parameters are used to describe the turbulent burning velocity [2, 3]. These are the local displacement speed s_d (and global displacement speed $\bar{s}_d$) and the local consumption speed s_t (and the global consumption speed $\bar{s}_t$). Each represents a useful way to characterise turbulent burning velocity on a local or global level. Measurement of the local consumption speed requires the measurement of mass fluxes, including the correlation $\rho'u'$, on all boundaries of a small control volume. For turbulent premixed flames, this approach is beyond experimental capabilities for the foreseeable future. Measurement of the local flame displacement speed s_d poses similar challenges. Here, the displacement of the flame front along the local normal needs to be resolved in time, requiring the simultaneous measurement of the flame front surface topology and the full convective velocity field both fully resolved in three dimensions.

In this paper we present a novel method to study the effects of turbulence on flame propagation, enabled by the combination of stereoscopic particle image velocimetry (SPIV) and time-sequenced planar laser-induced fluorescence imaging of OH-radicals. Using advanced image postprocessing algorithms, we extract a quantity which we refer to as s_d^{2D} and which describes the propagation of the reaction front under the influence of turbulence. s_d^{2D} is locally resolved along the flame front contour and is shown to be a sensitive indicator of flame-chemistry interactions. We explore the precision of the technique and potential systematic errors through experiment and simulations. The technique has the advantage of being realisable with current measurement technology, and a great advantage is that data from CFD-simulations can be analysed using identical post-processing algorithms. The sensitivity of s_d^{2D} to flame turbulence interactions can provide a critical test for computational codes and may thus be used both for validation of, and input to, numerical codes. Indeed, s_d^{2D} itself may be a useful quantity on which to base subgrid-scale (SGS) models in LES. The measurement technique we report is essentially two-dimensional in character and thus susceptible to artifacts when reporting on three-dimensional quantities (see [4]). One would thus not expect s_d^{2D} to be directly representative to the true flame displacement speed s_d. This point is explored in detail in the paper with Monte Carlo simulations and experiments, and conditions are suggested for which the quantities may be strongly correlated. The strengths of the method reported here lie in the relative simplicity of the experiments compared to attempts of resolving the full 3D-flamefront and velocity structure in time, and more importantly, the superior precision afforded by 2D-measurements.

The paper begins with an outline of theoretical concepts and a definition of s_d^{2D}. The principle of measuring s_d^{2D} is outlined, and possible artifacts intrinsic in 2D measurements and their effects on the determination of s_d^{2D} are discussed. Experimental details are discussed in Sect. 3. Image processing tools are described in Sect. 4 followed by a presentation of an example result and an uncertainty analysis (Sect. 5). Results are discussed in Sect. 6. The paper closes with a summary of the most important conclusions.

2 Theoretical concepts

The progression of the flame front is due to two components:

1. Movement of the flow field.
2. The progressive motion of the combustion reaction through the fluid. It is the latter that is characteristic of the local flame displacement speed s_d. This motion is effected by combustion chemistry and geometrical effects, decoupled from the turbulent flow field. It is strongly influenced by the local equivalence ratio. So far no direct experimental studies of s_d are available, although several investigations on flame front propagation have been reported in the literature, e.g. [5–11].

In this paper we present a novel approach to obtain s_d^{2D}. Measurements were performed in a bluff-body stabilised flame, and we present correlations of s_d^{2D} with various flame parameters for a number of flame conditions. Simultaneous use of stereoscopic particle image velocimetry (PIV) and time-sequenced OH-planar laser-induced fluorescence (PLIF) [12, 13] were used in conjunction with advanced post-processing routines to achieve this aim.

To aid the interpretation of experimental results, which will be presented later on, we provide a brief theoretical introduction to the general concept of flame displacement speed in relation to combustion modelling.

As reviewed in [14–16], the transport equation for fuel can be expressed in the kinematic form as

$$\frac{\partial Y_F}{\partial t} + u_i \frac{\partial Y_F}{\partial x_i} = s_d |\nabla Y_F|, \tag{1}$$

where u_i denotes the velocity of the fluid in direction i and Y_F the local fuel mass fraction. s_d is given as

$$s_d = \frac{\dot{w}_F - \nabla \cdot (\rho D \nabla Y_F)}{\rho |\nabla Y_F|}, \tag{2}$$

where $\dot{w}_F$ is the magnitude of the chemical reaction rate of the fuel, D the mass diffusivity and ρ the gas density. The density-weighted flame displacement speed is defined as [15–18]
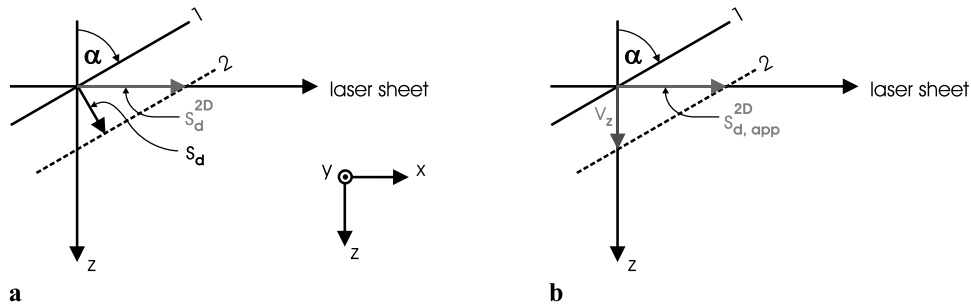
$$s_{d*} = \frac{\rho_F}{\rho_0} s_d, \tag{3}$$

Fig. 1 (**a**) Representation of the geometry used to define (8). The lasersheet travels from left to right along x and is parallel to the $x-y$ plane. The z-axis at is perpendicular to the laser sheet. Shown is an example where the flame front intersects the laser sheet at angle α. The measured 2D-displacement speed s_d^{2D} is a factor $(1/\cos\alpha)$ larger than the true displacement speed s_d. (**b**) Convection of the same flame front as shown in (**a**) with velocity v_z causes an apparent s_d^{2D} to be measured according to (9)

where ρ_0 is the unburned gas density and ρ_F the gas density at the position of the flame front. For an interpretation of the results on flame propagation behaviour shown in Sect. 5.1, it is useful to decompose the density-weighted flame displacement speed into its three components s_{r*}, s_{n*} and s_{t*} [19–21]:

$$s_{d*} = s_{r*} + s_{n*} + s_{t*}, \tag{4}$$

where s_{r*} is the reaction component:

$$s_{r*} = \frac{\dot{w}_F}{\rho_0 |\nabla Y_F|} \tag{5}$$

s_{n*} is the normal diffusion component:

$$s_{n*} = \frac{\vec{N}.\nabla(\rho D \vec{N}.\nabla Y_F)}{\rho_0 |\nabla Y_F|} \tag{6}$$

and $\vec{N}$ is the local flame normal.

s_{t*} is the tangential diffusion component:

$$s_{t*} = -2\rho D \kappa_m / \rho_0 \tag{7}$$

with κ_m the arithmetic mean of the two principal curvatures of the concerned surface [15]. The quantity we measure in the following paper is the projection of s_d onto the plane defined by the laser sheets intersecting the flame. In the case where the local flame surface normal propagates in a direction lying in the plane of the laser sheet, s_d and s_d^{2D} are the equivalent. However, for oblique angles, we have

$$s_d^{2D} = \frac{s_d}{\cos\alpha}, \tag{8}$$

where α is the angle between the flame surface normal and its projection onto the laser sheet plane. The geometry of this situation is illustrated in Fig. 1(a).

The bias caused by out of plane propagation is always positive leading to increases in s_d^{2D} compared to s_d. Thus for "oblique" propagation, α increases, and s_d^{2D} is larger than s_d. We will discuss the implications of this in forthcoming sections. A further artifact in the measurement of s_d^{2D} is caused by convection in the direction of z as shown in Fig. 1(b). For the same angle α between flamefront and light sheet, convection at speed v_z introduces an apparent displacement speed of $v_z \cdot \tan(\alpha)$. The measured displacement speed s_d^{2D} is thus related to the true displacement s_d as

$$s_d^{2D} = \frac{s_d}{\cos\alpha} + v_z \cdot \tan\alpha. \tag{9}$$

Note, however, that there is no loss of generality: The analysis methods developed in the present context can be applied in exactly the same way to computational data to extract s_d^{2D}, and, as we will show, s_d^{2D} is a sensitive general indicator of flame turbulence interactions and may even be used as the basis for the definition of sub-scale models.

3 Experimental methods

3.1 Burner

For this investigation, a 10-kW laboratory scale bluff-body stabilised combustor was used, which has been the subject of previous experimental and theoretical studies [22–26]. It was made up of a circular duct, 300-mm long with an inner diameter of 35 mm. The conical bluff-body anchoring the flame was 25 mm in diameter, giving a blockage ratio of 50%. In order to mimic combustion instabilities on a simple, well-controlled system, inlet velocity fluctuations were imposed on the bluff-body flame using two acoustic drivers (loudspeakers) mounted diametrically opposite of each other on the circumference of the burner plenum. The loudspeakers were excited with sinusoidal signals from a 40-MHz arbitrary waveform generator (TTI). The flame was acoustically forced at the eigenmodes of
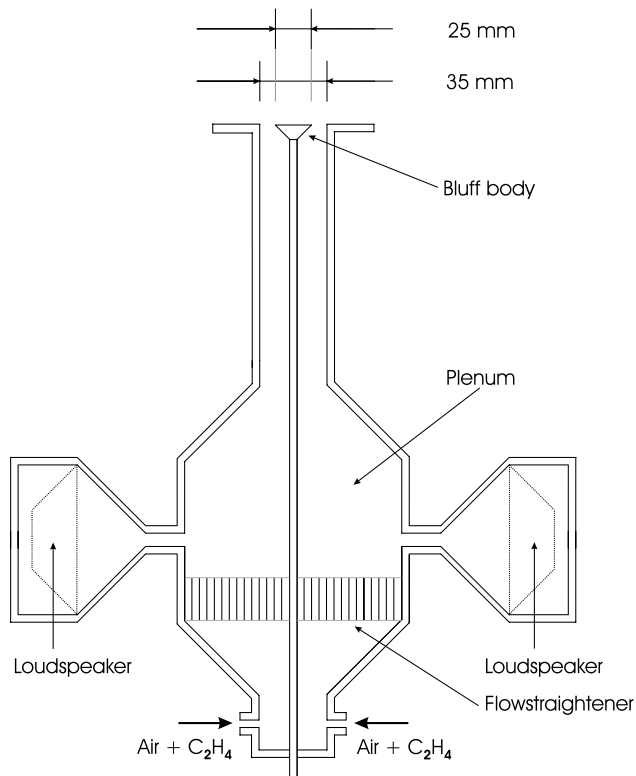
Fig. 2 Schematic representation of the acoustically forced bluf-body burner [23]

the plenum chamber which were 40, 160 and 310 Hz, respectively. When the flame was acoustically forced at a frequency of 160 Hz, a fluctuation of 65% on the mean inlet velocity was achieved. $u'/\bar{u}$ denotes the fluctuation over the mean inlet velocity (half peak to peak). Experiments were carried out with the combustor operating on premixed C_2H_4 and air at equivalence ratios ranging between 0.550 and 0.700 (Le > 1). A detailed description of the experimental settings are provided in Table 1 and will be described later on (Sect. 6). A schematic representation of the combustor is shown in Fig. 2.

3.2 Measurement techniques

Figure 3 shows a schematic of the diagnostic set-up for the combined double-shot OH-PLIF and stereoscopic PIV measurements.

3.2.1 OH-PLIF

The diagnostic system consisted of two Nd:YAG lasers (Continuum Surelite II) used as pump sources for one tunable dye laser (Sirah Cobra-Stretch). A high-resolution double-exposure ICCD camera (Lavision Nanostar) was used for the digital collection of the fluorescence signals to image the OH-PLIF signals. It was fitted with a UV f/4.5

camera lens (Nikkor) equipped with UG 11 and WG 305 filters (Comar). For spectral identification of the OH transitions, an LIF excitation scan was performed prior to the PLIF measurements. For OH LIF, the frequency-doubled output from one dye laser was tuned near 283 nm to excite the $Q_1(6)$ line in the $A^2\Sigma^+ - X^2\Pi(1,0)$ band. Pulse energies of 8 mJ were available from the dye laser at the excitation wavelengths, but the beams were spatially filtered yielding measured irradiance of $\sim$1.3 MW/cm^2 cm^{-1}, corresponding to the linear excitation regime. The laser beam was expanded into a sheet 50-mm high and 100-µm thick, using a cylindrical planoconvex lens with focal length of -25 mm and spherical lens with focal length of 500 mm. A region of 5 cm (width) × 4 cm (height) was imaged. The spatial power profile of the laser pulses was measured simultaneously with the PLIF signal. As shown in Fig. 3, part of the focused light-sheet was directed into a dye cell, which was filled with an aqueous solution of a fluorescent dye. The dye cell was positioned in such a way that the PLIF signal and the fluorescent dye were in focus on the ICCD-chip. The dye fluorescence was imaged onto a strip of approximately 100 pixels in width to one side of the ICCD-chip to provide an instantaneous beam power profile measurement.

The ICCD camera was capable of acquiring two images in rapid succession. This enabled the measurement of two OH-PLIF images in short separation. To achieve this, the camera intensifiers were gated to open for 350 ns for the PLIF measurements. The time delay possible to employ in order to choose between the two laser pulses was 150 µs. This delay resulted in a movement of the flame front of about 15 pixels. s_d^{2D} was found to be in the range of 20% of the overall flame front displacement. Thus, this was the minimum delay to resolve s_d^{2D}. Since the laser dye solution could not recover from the first laser pulse within these 150 µs, the spatial power profile of the second laser pulse was seen to be affected by the first laser pulse, making shot-by-shot beam profile referencing essential.

3.2.2 Stereoscopic PIV

Stereoscopic PIV was performed to characterise the velocity fields of both unburnt and burnt gases from the flame. The second harmonic from a pulsed Nd:YAG (Big Sky Laser Technologies Inc., Ultra #1, 35 mJ/pulse) was used to create a light-sheet of 480-µm thickness (FWHM). The PIV-lasers and PIV-cameras were triggered from a PIV-synchroniser (ILA, Germany), which in turn was triggered from a 40-MHz arbitrary waveform generator (TTi). Both cameras (Sensicam, PCO imaging, Germany, 1280 × 1024 pixels, double-frame mode) were arranged at 90° with the lenses arranged according to the Scheimpflug criterion. Each camera was fitted with a narrow bandpass interference filter (centred at 532 nm with 10 nm FWHM; max.

Fig. 3 Set-up for combined OH-PLIF and stereoscopic PIV measurements performed. Description of components: *PIV*—particle image velocity; *PLIF*—planar laser induced fluorescence; *CCD*—charge-coupled device camera, *ICCD*—intensified CCD camera; *f*—focal length
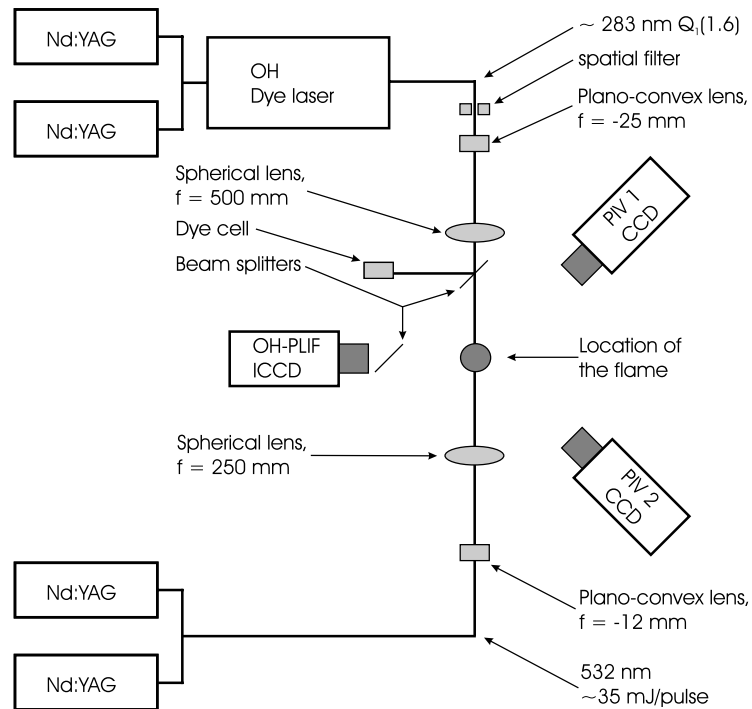
transmission = 90%) to reject flame emission. The separation between the PIV laser pulses was 15 μs. Particles (SiO_2, primary diameter 12 nm, Aerosil R 812, Degussa, Germany) were seeded into the reactive mixture with a fluidised bed followed by a cyclone and a choke to select only the smallest particles (<1 μm) and dissociate large agglomerates. The PIV laser sheets were overlapped with the OH-PLIF sheets in a counterpropagating configuration as shown in Fig. 3.

The "Davis 7.1" processing software (Lavision, Germany) was used for velocity calculations. After subtracting the minimum intensity level in each double frame image, the data were cross-correlated at successively smaller interrogation areas leading to a discrete window offset [27]. After each pass the peak-ratio from the cross correlation (ratio of highest to 2nd highest peak in the correlation plane: ≥1.8) and the change of velocity with respect to the standard deviation were used to remove invalid vectors and to interpolate between them. After the final cross-correlation, using an interrogation region of 8 × 8 pixels without overlap, which corresponds to 274 × 274 μm, and window filtering the data were subjected to a 3 × 3 Gaussian smoothing operation. Finally, the two velocity fields extracted from the two individual cameras were combined to yield three-component velocity vectors. On average more than 99% valid vectors were obtained in the particle seeded field of view. One of the advantages of using stereoscopic PIV is that regions of strong 3D-flow character, where the calculated flame displacement speeds are invalid because they are obtained with a 2D-measurement technique, can be directly identified and excluded from statistical analysis.

3.2.3 Triggering

A 40-MHz arbitrary waveform generator was used to provide a 2-Hz signal which represented the main trigger signal for OH-PLIF, 3D-PIV and the forcing of the loudspeakers in the burner. Images were acquired phase resolved at a frequency of 1 Hz and images for OH-PLIF and PIV saved on two different PCs. A sequence of images was started with an OH-PLIF image ($t = 0$ μs). A delay of 500 ns was set between the first OH-PLIF image and the first PIV-image ($t = 0.5$ μs) to avoid potential interferences between the laser pulses and cameras. At the given bulk velocities and with the spatial resolution of the optical set-up, the chosen delay of 500 ns between the pulses rendered these measurements virtually instantaneous on flow timescales. The spacing between both PIV-laser pulses was chosen to be 15 μs (second PIV-laser pulse at $t = 15.5$ μs), which resulted in a displacement of the seeding particles between 0 and 10 pixels in this time frame. The second OH-PLIF laser was triggered at $t = 150$ μs, which resulted in a maximum flame front displacement of about 15 pixels.

4 Image processing

4.1 Preprocessing

Information on flamefront position from OH-PLIF images, together with information on the velocity field from PIV-images, allows the flame-displacement speed to be calcu-

Fig. 4 One single shot of an OH-PLIF image shown at various steps of postprocessing: (**a**) Original image with background subtracted; (**b**) OH-PLIF image corrected for beamprofile of incident laser beam with simultaneously acquired power distribution within the laser sheet; (**c**) After application of nonlinear diffusion filtering. Flamefront obtained with Canny edge detection superimposed is shown in black; (**d**) OH-images binarised into burnt and unburnt regions. Images III and IV are mapped onto the PIV-coordinate system and are thus mirrored
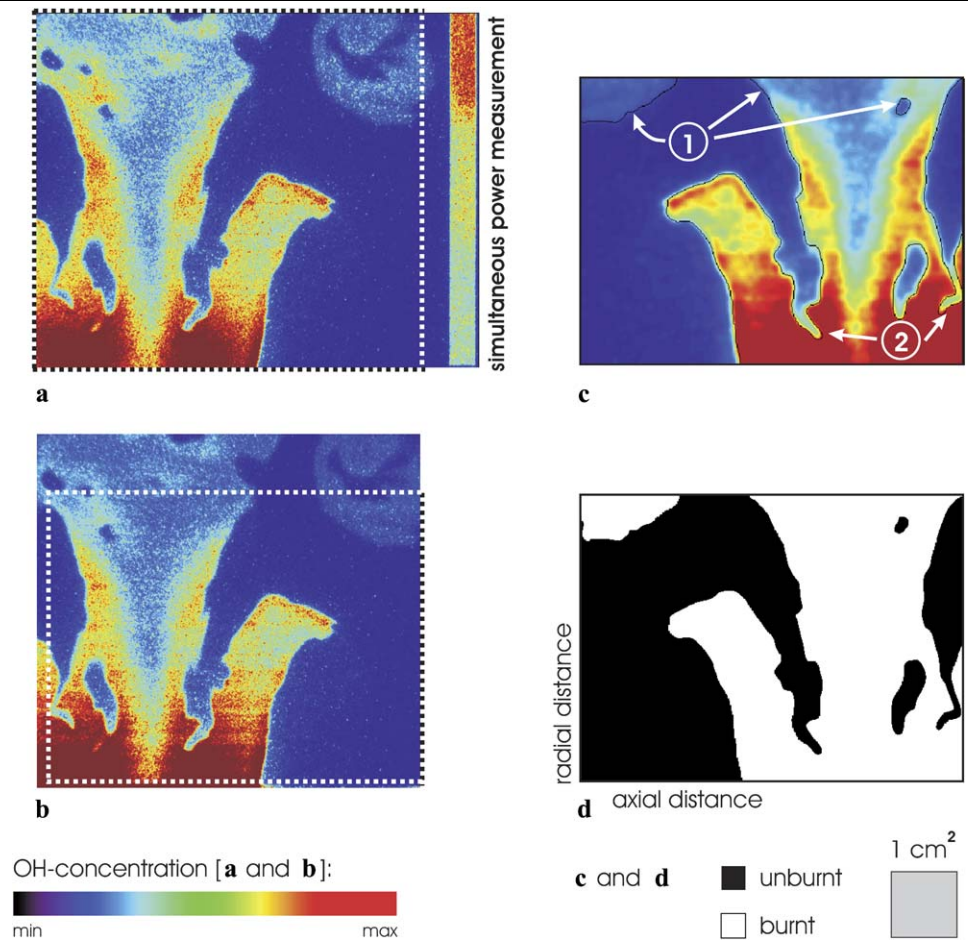
lated. Details of the procedure are as follows: First, a background image, measured in the absence of the flame, was subtracted from the fluorescence images (Fig. 4(a)). Second, these images were corrected for laser sheet inhomogeneities using the instantaneous laser power profile recorded with each image. Stretch, rotation and vertical shift between the instantaneous power profile image and the OH-image were corrected for (Fig. 4(b)). Third, an anisotropic nonlinear diffusion filter was applied [28] to reduce the level of noise and to enhance gradients in the images. The method has several advantages: Noise is smoothed locally within regions defined by object boundaries, whereas little or no smoothing occurs between image objects. Local edges are enhanced because discontinuities, such as boundaries, are amplified. Mathematically one treats the problem as a diffusion process, where the diffusion coefficient is adapted locally to the effect that diffusion stops as soon as an object boundary is reached. Fourth, these images were resized to 50% of their original size yielding a signal-to-noise ratio gain of around 4. Fifth, the Canny edge detection algorithm [29] was applied to find the flame front contour. Since the displacement of the flamefront is in the order of 15 pixels of which the chemical contribution to the flame displace-

ment (see Sect. 4.2) is only in the range of about 3 pixels, it is essential to select the position of the flame front with great care. The position of the flamefront was chosen as the position of the maximum gradient in the OH-field. Via the Canny edge detection algorithm the contour defining the maximum gradient in the OH distribution is selected. This was found to lead to a systematically more reproducible definition of a flame front contour than using a constant threshold algorithm as is often reported in the literature. In the latter one simply binarises images into unburnt and burnt regions with the interface between these regions taken to be the flamefront location. The problem with this method is that signal-to-noise ratios in images vary widely both due to beam profile inhomogeneities and also variations in OH concentration. In the present configuration we observed that this could lead to uncertainties of up to 10 pixels, which is too large for meaningful extractions of s_d^{2D}. This is illustrated in Fig. 4(c), where the flame fronts are resolved well in regions of low signal-to-noise ratio [①] as well as regions of high signal-to-noise ratio [②]. Sixth, the images were binarised in unburnt and burnt along the maximum gradient. Seventh, the PLIF image and PIV-images were aligned and superimposed on a pixel-by-pixel basis. This alignment is essential

to the success of this image technique because of the small spatial scales of reacting layers in the flame. This warping procedure was performed in several stages. First, both laser sheets were aligned to exactly overlap in the measurement plane. Second, a target image (cross pattern) was aligned in the measurement plane, defined by the laser sheets and in the view of all three cameras. Third, the coordinates of 90 reference points on the target image were captured by both PIV-cameras, dewarped in the PIV software (LaVision) and both images superimposed (= image A). The PLIF-image (= image B) taken of the same target was mirrored, and the corresponding coordinates of 90 reference points were identified. Custom software was written in IDL [30] to map coordinates of Image B onto image A. For this, a transformation matrix relating the two sets of coordinates was calculated and used to map image B onto the coordinate system of image A (Fig. 4(c and d)). The precision of this technique is in the subpixel range [31]. These operations reduced the OH-pixel resolution by 6% from 86 μm to 92 μm. The vector field was enlarged by a factor of 3 in a bicubic interpolation scheme to match the matrix size of the OH-field. Then s_d^{2D} was calculated as described in the next section. Flame surface densities (FSD) were also calculated using procedures previously described in [23].

4.2 Calculation of s_d^{2D}

s_d^{2D} was calculated using information about the flame contour which was obtained from the OH-images and the velocity field gained from stereoscopic particle image velocimetry. Figure 5 schematically illustrates the calculation procedure.

In the following the OH-image at $t = 0$ μs is referred to as frame 1 and the OH-image at $t = 150$ μs as frame 2. In each OH-frame the corresponding flame contours were obtained via edge detection. The flame contours within an image, corresponding to each other, were each sorted to a line of adjacent pixels. If the PLIF images are binarised into burnt/unburnt regions, then a superposition of frame 1 and frame 2 will show a region which is burnt in both images (region A); a region which is still unburnt in frame 1 but burnt in frame 2 (region B); and a region which is unburnt in both frames (region C). The borderline from region A to region B marks flamefront 1 (flame contour of frame 1) and the borderline from region B to region C flamefront 2 (flame contour of frame 2). To isolate the displacement of the flamefront due to convection, the velocity field is followed until 150 μs have passed for each flame contour pixel of frame 1 (Fig. 5; pixel marked A). This latter step is implemented as follows: First, from v_x and v_y the direction of the velocity field is determined. Second, the exact position of the new location with unity length 1 (1 pixel $\triangleq$ 91.7 μm) in this direction is calculated. Third, the time necessary to

pass this distance t_p is calculated, which is obtained from the absolute length of the velocity vector $v_{xy} = \sqrt{v_x^2 + v_y^2}$ at the rounded pixel position from step 2. Steps 1 to 3 are iterated until 150 μs have passed. For each subsequent iteration step, (a) step 1 uses the rounded pixel position of step 2 from the last iteration; (b) the new pixel position in step 2 is not calculated from the rounded old pixel position, but from the precise position. The rounded pixel position of the final iteration is referred to as the *convection pixel* (Fig. 5; pixel marked A'). The information about the length of the path (Fig. 5; distance from A to A') represents the contribution to the flame displacement which is only due to convection.

This analysis assumes that local flow *patterns* do not change significantly over the measurement time (150 μs) although they are subject to the overall convective motion of the flow. The effect is mostly a global displacement of local flow patterns. A full quantification of the evolution of turbulent flow structures would require a sequentially resolved velocity measurement technique. This would add significantly to complexity and cost of the experiment. However, recent evidence from cinematographic PIV measurements do indeed suggest that local flow patterns are not changing significantly in character over the short measurement time scale between the two OH measurements [32, 33].

The distance of the *convection pixel* to a corresponding pixel in frame 2 (Fig. 5; distance from A' to A'') represents the "chemical" flame displacement. However, due to strong wrinkling at high acoustic forcing of the flame, the corresponding pixels in frame 2 may not necessarily be simply those located at the minimum distance from a given *convection pixel*. This is depicted in Fig. 6(a) for an extreme case. It shows a section of the *convection line* in green, and imaged flamefront 2 in red. It can be clearly seen that the black vectors, representing the shortest distance from each *convection pixel* to a pixel in flamefront 2, represent an implausible evolution of the flame shape. Therefore we proceeded as follows: First, each pixel along the convection line m_c and flame front 2 m_{f2} was numbered sequentially, yielding two "coordinate vectors" $m_{c,n} = [1, 2, \ldots, k]$ and $m_{f2,n} = [1, 2, \ldots, m]$, where the matrix denominated with index n contains numbered coordinates rather than x & y coordinates. Then displacement vectors were calculated corresponding to the minimum distance between the *convection line* pixels and pixels in flamefront 2, as explained above. The arrival coordinate of each flame displacement vector ($m_{d,\text{temp}}$) is an element of vector m_{f2}. Corresponding starting coordinate and arrival coordinate of a flame displacement vector are written in an horizontal row. Thus vector $m_{d,\text{temp}}$ has k elements. A new vector $m_{d,\text{temp},n}$ was then created of length k containing the "target coordinates" of $m_{f2,\text{temp}}$, which it has in m_{f2}, in a numbered order. In regions of strong wrinkling this would occasionally lead to "misassignments" leading to problems of the type

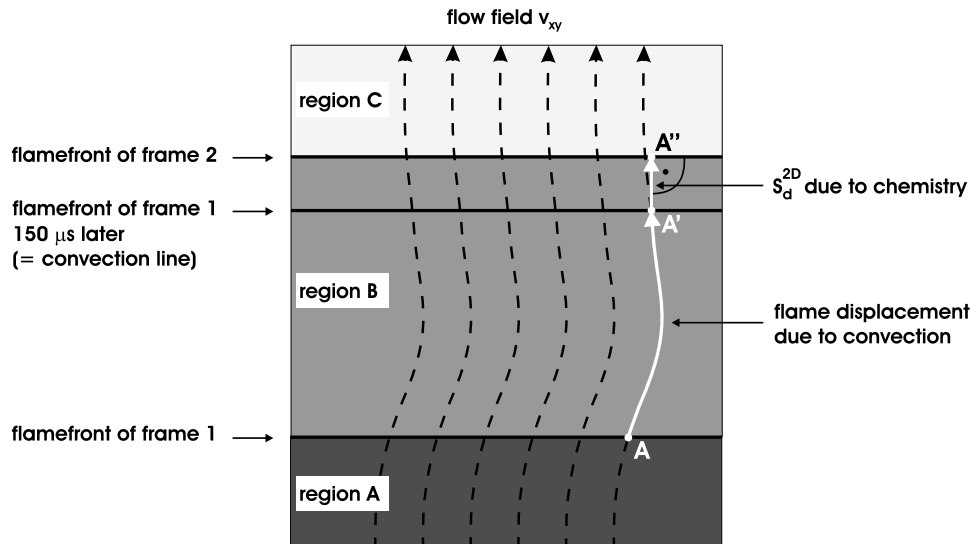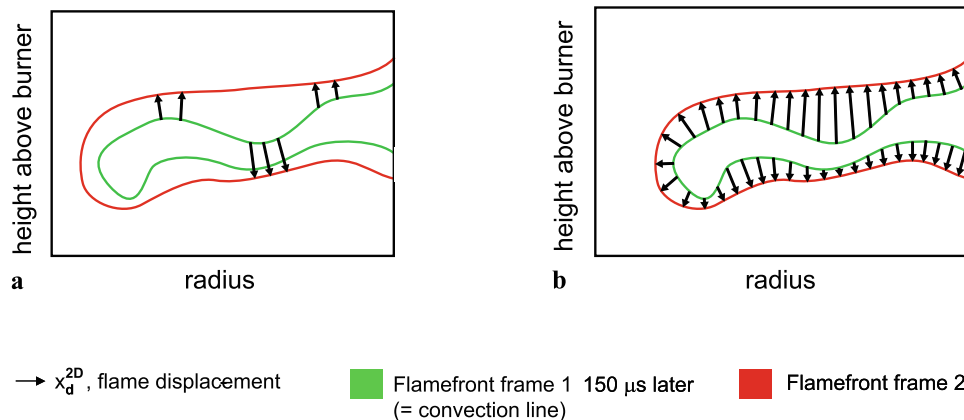**Fig. 5** Illustration of the principle for the calculation of s_d^{2D}

Fig. 6 Finding the correct flame displacement in strong wrinkled regions within the flame. Example displacement vectors: (**a**) "minimum path difference algorithm" applied without optimisation algorithm; (**b**) with optimisation algorithm

illustrated in Fig. 6(a). Such misassignments are identifiable in $m_{d,\text{temp},n}$ as regions where coordinates do not increase monotonically. In these regions a local interpolation scheme was applied that led to a "reordering" of coordinates ($m_{d,n}$) and subsequently m_d. This allowed the final s_d^{2D} vectors (m_{FDS}), which were used for statistical analysis, to be calculated. The final s_d^{2D}-vector-plot is illustrated in Fig. 7 below. The result of this scheme appears satisfactory even in strongly wrinkled regions as illustrated in Fig. 6(b). In regions of high local turbulence additional parts of the flame front had to be excluded for statistical analysis due to the impossibility of reconstructing the evolution of the flame front. An example of this is when a flame region breaks apart into two or more flame islands. This results in an exclusion of data not considered for the statistical analysis of less than 1% for flame cases (a) to (f), about 2% in flame case (g) and 6% in flame case (h) in addition to the exclusion of the flame front locations with $v_z > 2$ m/s, as will be described below.

An additional postprocessing step was applied to ensure that flame displacement vectors pointing to flamefront 2 are evenly distributed over the pixels of flamefront 2. Figure 8 shows an image before (a) and after (b) the application of this post processing step.

Large out-of-plane convection can lead to artificially high values for s_d^{2D}, increased by the amount $v_z \cdot \tan \alpha$ as shown in (9). In the present experiments the application of SPIV is therefore essential, so that regions with large v_z-components can be excluded. Locations along the flame front for which $|v_z| > 2$ m/s were excluded from analysis. The fraction of pixels disregarded from statistical analysis due to $|v_z| > 2$ m/s was 3% for flame-setting (b) and 6% for flame-setting (h). The effects of v_z on errors in s_d^{2D} will be explored in the next section to motivate this cut-off value. It is worth to mention at this stage related work exploring problems with out-of-plane motion on 2D-flame measurements ([4]). More will be said in this context in the uncertainty analysis in the next section.
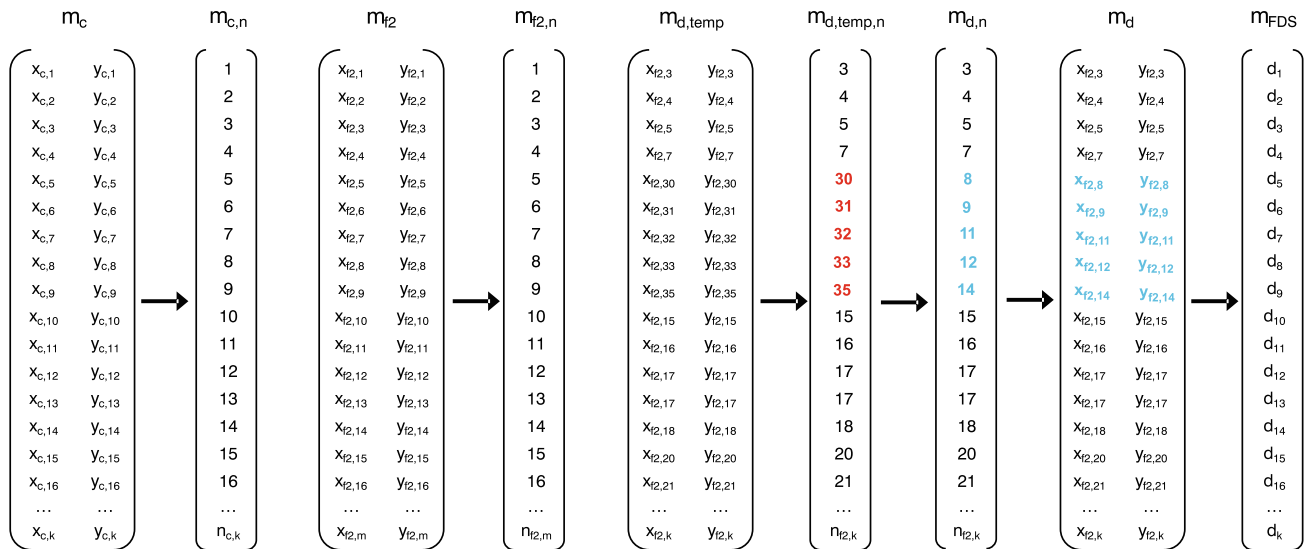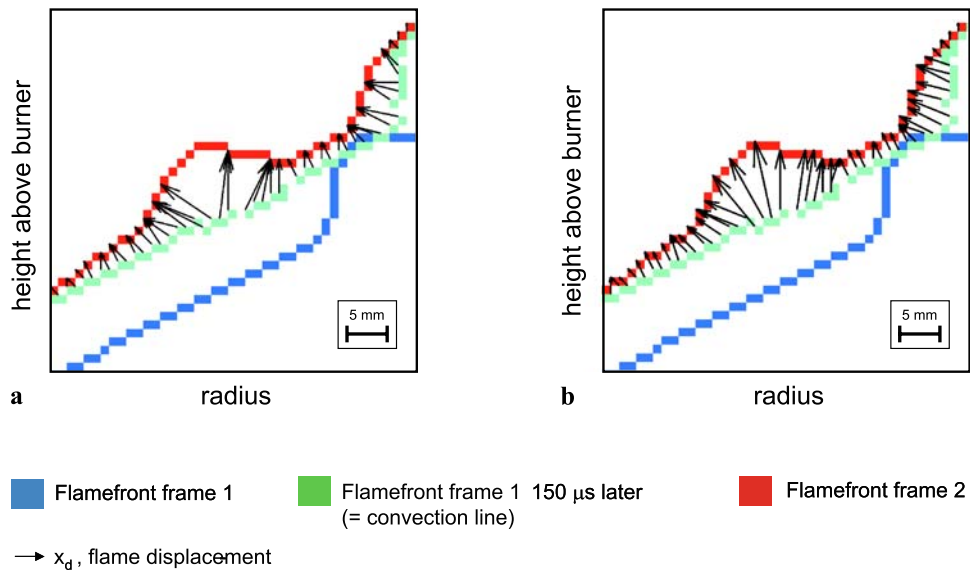
m_c		$m_{c,n}$	m_{f2}		$m_{f2,n}$	$m_{d,temp}$		$m_{d,temp,n}$	$m_{d,n}$	m_d		m_{FDS}
$x_{c,1}$	$y_{c,1}$	1	$x_{f2,1}$	$y_{f2,1}$	1	$x_{f2,3}$	$y_{f2,3}$	3	3	$x_{f2,3}$	$y_{f2,3}$	d_1
$x_{c,2}$	$y_{c,2}$	2	$x_{f2,2}$	$y_{f2,2}$	2	$x_{f2,4}$	$y_{f2,4}$	4	4	$x_{f2,4}$	$y_{f2,4}$	d_2
$x_{c,3}$	$y_{c,3}$	3	$x_{f2,3}$	$y_{f2,3}$	3	$x_{f2,5}$	$y_{f2,5}$	5	5	$x_{f2,5}$	$y_{f2,5}$	d_3
$x_{c,4}$	$y_{c,4}$	4	$x_{f2,4}$	$y_{f2,4}$	4	$x_{f2,7}$	$y_{f2,7}$	7	7	$x_{f2,7}$	$y_{f2,7}$	d_4
$x_{c,5}$	$y_{c,5}$	5	$x_{f2,5}$	$y_{f2,5}$	5	$x_{f2,30}$	$y_{f2,30}$	30	8	$x_{f2,8}$	$y_{f2,8}$	d_5
$x_{c,6}$	$y_{c,6}$	6	$x_{f2,6}$	$y_{f2,6}$	6	$x_{f2,31}$	$y_{f2,31}$	31	9	$x_{f2,9}$	$y_{f2,9}$	d_6
$x_{c,7}$	$y_{c,7}$	7	$x_{f2,7}$	$y_{f2,7}$	7	$x_{f2,32}$	$y_{f2,32}$	32	11	$x_{f2,11}$	$y_{f2,11}$	d_7
$x_{c,8}$	$y_{c,8}$	8	$x_{f2,8}$	$y_{f2,8}$	8	$x_{f2,33}$	$y_{f2,33}$	33	12	$x_{f2,12}$	$y_{f2,12}$	d_8
$x_{c,9}$	$y_{c,9}$	9	$x_{f2,9}$	$y_{f2,9}$	9	$x_{f2,35}$	$y_{f2,35}$	35	14	$x_{f2,14}$	$y_{f2,14}$	d_9
$x_{c,10}$	$y_{c,10}$	10	$x_{f2,10}$	$y_{f2,10}$	10	$x_{f2,15}$	$y_{f2,15}$	15	15	$x_{f2,15}$	$y_{f2,15}$	d_{10}
$x_{c,11}$	$y_{c,11}$	11	$x_{f2,11}$	$y_{f2,11}$	11	$x_{f2,16}$	$y_{f2,16}$	16	16	$x_{f2,16}$	$y_{f2,16}$	d_{11}
$x_{c,12}$	$y_{c,12}$	12	$x_{f2,12}$	$y_{f2,12}$	12	$x_{f2,17}$	$y_{f2,17}$	17	17	$x_{f2,17}$	$y_{f2,17}$	d_{12}
$x_{c,13}$	$y_{c,13}$	13	$x_{f2,13}$	$y_{f2,13}$	13	$x_{f2,17}$	$y_{f2,17}$	17	17	$x_{f2,17}$	$y_{f2,17}$	d_{13}
$x_{c,14}$	$y_{c,14}$	14	$x_{f2,14}$	$y_{f2,14}$	14	$x_{f2,18}$	$y_{f2,18}$	18	18	$x_{f2,18}$	$y_{f2,18}$	d_{14}
$x_{c,15}$	$y_{c,15}$	15	$x_{f2,15}$	$y_{f2,15}$	15	$x_{f2,20}$	$y_{f2,20}$	20	20	$x_{f2,20}$	$y_{f2,20}$	d_{15}
$x_{c,16}$	$y_{c,16}$	16	$x_{f2,16}$	$y_{f2,16}$	16	$x_{f2,21}$	$y_{f2,21}$	21	21	$x_{f2,21}$	$y_{f2,21}$	d_{16}
...	...	...	...	...	...	...	...	...	...	...	...	...
$x_{c,k}$	$y_{c,k}$	$n_{c,k}$	$x_{f2,m}$	$y_{f2,m}$	$n_{f2,m}$	$x_{f2,k}$	$y_{f2,k}$	$n_{f2,k}$	$n_{f2,k}$	$x_{f2,k}$	$y_{f2,k}$	d_k

Fig. 7 Visualisation of procedure to obtain corresponding s_d^{2D}-vectors under high forcing conditions

Fig. 8 Postprocessing of obtained flame displacement vectors: (**a**) without postprocessing; (**b**) with postprocessing

Flamefront frame 1

Flamefront frame 1 150 μs later (= convection line)

Flamefront frame 2

x_d , flame displacement

# 5 Example result and uncertainty analysis

5.1 Example result

An example image analysed according to the procedures outlined in the previous sections is shown in Fig. 9(b), which gives an impression of the full field of view. The area highlighted by the rectangle in the image is shown magnified in Fig. 9(a) demonstrating the high spatial resolution achieved by the method.

The *convection-line* has a shape mimicking the contour of flamefront 2, which is indicative of the fact that the major displacement of the flame front is due to convective transport. Differences are however due to geometrical effects and combustion chemistry. The black vectors in the figure are the flame displacement velocities providing magnitude and direction of the s_d^{2D}. An impression on the variability of s_d^{2D} within an image is obtained on inspection of Fig. 9(b). A strong vortex is seen near the centre of the image in Fig. 9(b), leading to a strong contortion of the flamefront. It is in this region that the largest variability of s_d^{2D} can also be seen presumably due to strong curvature of the flamefront [34]. On average an s_d^{2D} of 1.7 m/s was obtained, which will be referred to as the global displacement speed $\bar{s}_d^{2D}$. Note that this speed is not density weighted and does not therefore take into account a contribution to s_d^{2D} of gas expansion due to the temperature rise at the flamefront (see discussion further down and also [15, 16, 21]). More on this will be said in Sect. 6.

Fig. 9 Example image of s_d^{2D}
(flame setting f) in Table 1.
(**a**) shows a small region of the
flame. (**b**) shows the whole of
one side of the flame which was
recorded
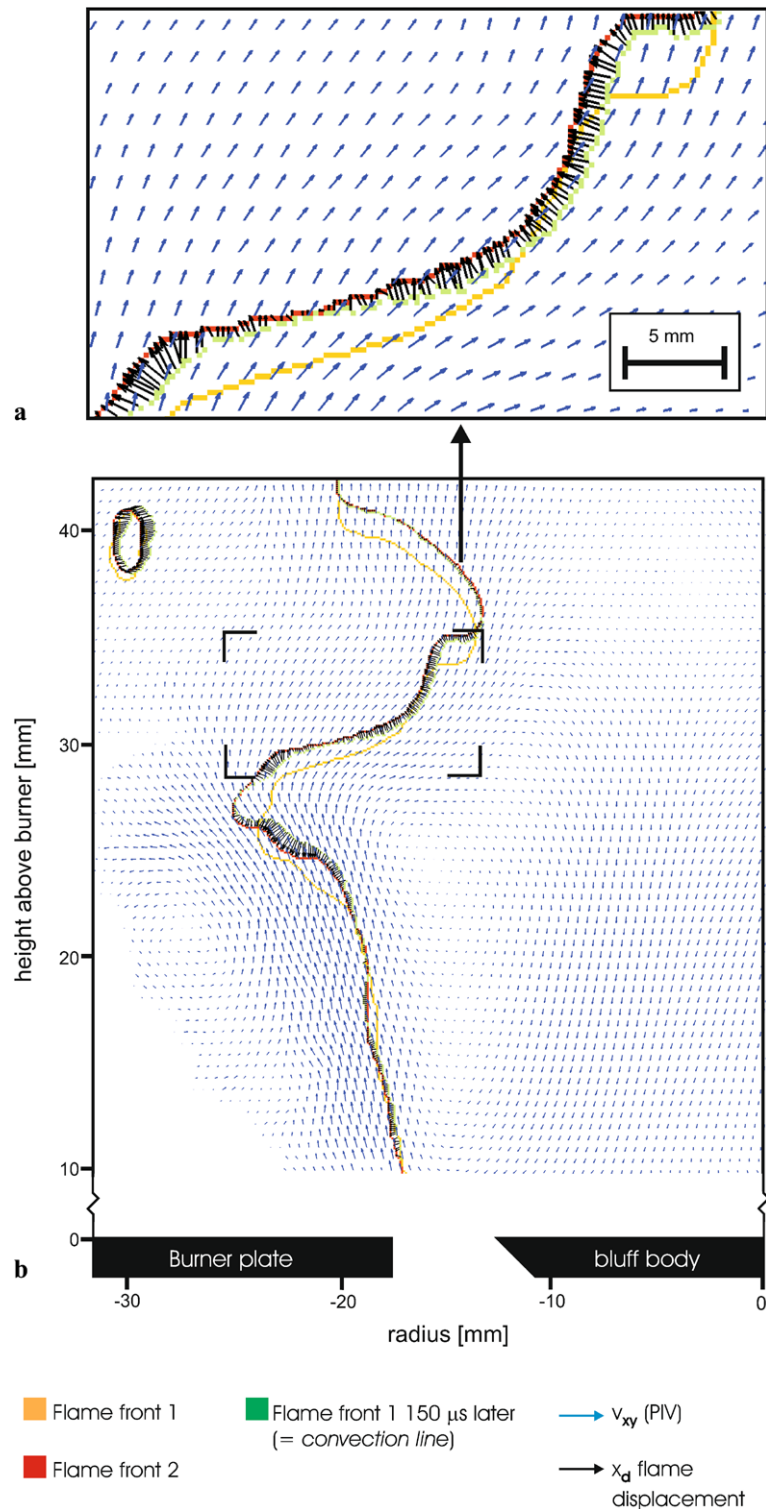
5.2 Experimental uncertainties

The uncertainty on the magnitude of the obtained s_d^{2D} arises from uncertainties in obtained velocity fields, determination of the local front position and the warping of the velocity fields obtained by PIV onto the flamefront contours obtained

from OH PLIF. The uncertainty of velocity measurement for v_x and v_y is estimated to be less than ± 0.5 m/s following the approach of Rehm [35] based on an error estimate in the pixel position of the *convection-line* of 1.5 pixels. The uncertainty of the flamefront pixel position in regions of negative, negligible and small positive curvature is about ± 0.5 pixels,

which is mainly due to errors in the warping-procedure of the binarised OH-image. In regions of large positive curvature, especially if both flame contours are close to one another (e.g. as occurs in a pocket of entrained air), this error may be larger as the pixel position of the flame contour is less precise. A high gain setting of the ICCD-camera was needed because of double pulse pumping of the dye laser, giving lower than normal output powers and a deteriorated beam profile. The high gain leads to some "flattening" of intensity gradients in strongly positively curved regions. As a consequence, the precision of which the maximum gradient is located by the Canny edge detection algorithm will be reduced. Combining errors, we estimate maximum errors in s_d^{2D} to be around ± 0.6 m/s. Whilst this error for individual displacement vectors is substantial, it has to be realised that for the statistical analyses presented in the results, 65,000 data points are included. Note, that the uncertainty in s_{d*}^{2D} compared to s_d^{2D} is lower by a factor of 4.6 to 5.1 (see explanation below) and thus around ± 0.12 m/s.

5.3 Effects of flame geometry on s_d^{2D}

The three-dimensional character of flamefronts and its effect on velocity measurements has been the subject of detailed past investigation. In particular the topic of optical flow velocimetry (OFV) technique has been critically examined in this context. Here one measures the correlation between (often diffuse) brightness features in sequentially acquired images to infer flow velocities. In a detailed study comparing OFV and PIV Fielding et al. [4] found substantial deviations both between the directions of corresponding PIV and OFV flow vectors and also relative velocity differences. Whilst much of their discussion is relevant to the present paper, there are important differences: In contrast to OFV, we are not here tracking continuously varying and mostly diffusive scalar features to obtain gas phase velocity data. Indeed much of the error associated with OFV was found to stem simply from the difficulty in distinguishing diffusive image features as interrogation regions were decreased in size. The resulting correlation maps were much less conclusive than the corresponding, sharply peaked, correlation maps obtained from PIV (where discrete image objects are being tracked). In the present case we are merely tracking the sharply defined contour of the flame itself, which is clearly and discretely separated in the two image frames. Systematic errors may however still arise in our case due to ambiguities in the method of connecting corresponding pixels on the convection line with those on flamefront 2 (4.2). These ambiguities are small because of the small displacements we measure between the convection line and flame contour 2, and both contours are geometrically self similar over the time period investigated. Whilst the difficulty of merely "tracking" the flame contour is a much simpler prob-
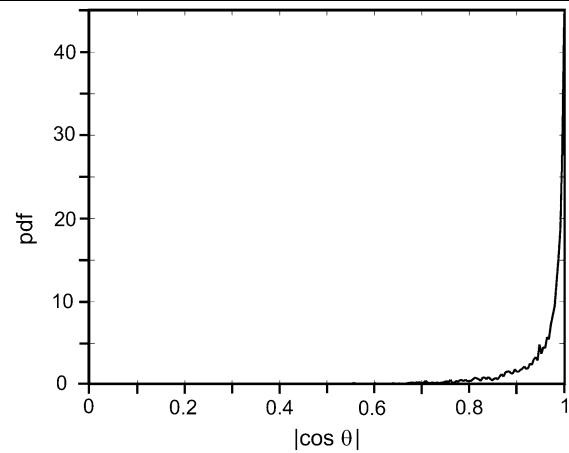

Fig. 10 Pdf of flame normal alignment with the fluid velocity v_{xy}

lem than velocity tracking in OFV, the effects of large out-of-plane motion leads to similar problems in both cases. As discussed, in the theoretical section (see Sect. 2), convection of large scale structures into (and out of) the measurement plane causes an "artificial" flamefront displacement of magnitude $v_z \tan \alpha$ with α defined as in (8) and Fig. 1 above. The quantity is negative or positive depending on whether the motion is into or out of the measurement plane. Thus for the case that $v_z \tan \alpha < s_d^{2D}$, this would merely introduce symmetrically distributed scatter on the evaluated s_d^{2D}. Correlations between s_d^{2D} and v_z revealed that this was indeed the case. Of course even if the convective components lie completely in the plane defined by the laser sheet, turbulent wrinkling could lead to the flamefront normal n to be in a direction that points out of this plane. Effects of v_z on s_d^{2D} will be investigated in more detail with Monte Carlo simulations in Sect. 5.4.

Even if all *convective* components are in plane with the laser sheet, the chemical component to the flame displacement could be in a direction that is not in the plane of the laser sheet. For this situation, s_d^{2D} would differ with respect to the true s_d according to (8). An estimate of this effect can be obtained by comparing the angles between the *in plane* component of n (the flamefront normal) with respect to the determined s_d^{2D}. Such a correlation is shown in Fig. 10, and indeed one finds that the alignment between the flamefront normal and the local flow velocity components is very strongly correlated. This is not altogether unexpected as the higher viscosity of the combustion gases leads to a local alignment of the scalar gradient with respect to the flow field.

5.4 Estimation of true displacement speeds s_d from 2D-measurements

Measurement of the true displacement speed requires one to measure the temporal evolution of the flamefront normal as

well as the flow field evolution in three-dimensional space. This, however, is beyond the scope of current measurement technology. In any case the uncertainties involved in such a measurement would offset the likely benefits of such an approach. As we show, the measurement of s_d^{2D} is feasible and valuable in the context of CFD-validation and model input, because these model data can be analysed in an analogous fashion. Nevertheless, it is interesting to estimate to which degree the statistics of s_d^{2D} might be representative of those for the truedisplacement speed s_d. These uncertainties can be approximated by use of (9) and assumed pdfs for α (as defined in Fig. 1). Using the measured pdfs for v_z and s_d^{2D} we performed Monte Carlo simulations to reconstruct pdfs for s_d.

Figure 11 shows comparisons between s_d and s_d^{2D} based on the assumed angle distributions for α shown in the first column. The second column shows the measured pdf for v_z. The last column compares the pdfs for the measured s_d^{2D} with those for the true flame displacement speed s_d for different α distributions. In (a) α is assumed to follow a Gaussian distribution with an FWHM of 35°. In (b) the measured pdf of v_z is shown which extends over the interval $-2.0 \le v_z \le 2.0$ m/s (as explained in Sect. 4.2, data outside this range were ignored in the calculation of s_d^{2D}). In (c) the corresponding pdfs for s_d^{2D} (wide black bars) and s_d (thin grey bars) are plotted. s_d was modelled by Monte Carlo simulations based on (9), using the experimentally obtained pdfs for v_z and s_d^{2D} and the assumed pdf for α. As seen in (c) there is remarkable similarity between s_d and s_d^{2D}. The insets (d), (e) and (f) explore pdfs for s_d for three individual velocity classes (bins) of s_d^{2D}, $0.6 \le s_d^{2D} \le 0.9$ m s, $3.0 \le s_d^{2D} \le 3.3$ m s and $6.0 \le s_d^{2D} \le 6.3$ m/s, respectively. The bin sizes for the plots shown in (d) to (f) are 0.3 m/s and identical to the bin sizes in (c). The arrows indicate the position of the s_d^{2D} bin for which s_d is investigated. As seen the angular spread in α causes some "spill over" into adjacent bins (for $\alpha = 0$, the pdfs for s_d^{2D} and s_d would be identical). The widths of the pdfs in (d) to (f) are, however, relatively small and almost symmetrically distributed. Some asymmetry is evident for the highest speed (shown in (f)) exhibiting a bias towards lower magnitudes of s_d. This is expected since for large values of α, the first term on the rhs of (9) will lead to strong bias to high velocities in s_d^{2D}.

Figures 11(g) to (l) show the corresponding plot for an FWHM of 70° of α. Here significant bias is seen for s_d as s_d increases. The effect is that s_d^{2D} exhibits a broader shoulder towards larger magnitudes.

In Figs. 11(m) to (r) we assume that the statistics of the out-of-plane orientation α are identical to the in-plane orientation of the flame sheet. The pdf shown in Fig. 11(m) is calculated from the angle (β) between s_d^{2D} and the normal of the mean-progress-variable in the laser-sheet plane. If we assume that such a pdf mimics the distribution for α,

the pdfs for (o) to (r) are obtained. Although there is clearly some bias towards high velocities, there is still remarkable similarity between the pdfs of s_d and s_d^{2D}. This assumption of isotropy may not be unreasonable and has been discussed before e.g. in [36], where similar widths for the angular distribution were found.

In Figs. 11(s) to (x) we explore whether the choice of the cut-off value for v_z used in the analysis presented here (cut-off: $|v_z| > 2$ m/s) has impact on the observed statistics of s_d^{2D} and s_d. If their pdfs change shape (i.e. narrow) significantly for smaller cut-off values, the high out-of-plane velocities must have a strong impact on the measured statistics. Figures 11(s) to (x) show that this is not the case: For a lower cut-off frequency of $|v_z| > 1$ m/s (Fig. 11(t)), the pdfs for s_d^{2D} and s_d are hardly different (comparison of Fig. 11(u) with Fig. 11(i)). A closer inspection of individual velocity bins (comparison of Figs. 11(v) to (x) with Figs. 11(j) to (l)) show only minor narrowing of the lower threshold value.

Figure 12 plots the ratio v_{xy} to v_z for flame setting (b). This pdf peaks at a ratio of v_{xy}/v_z of 8 and clearly illustrates that the flow field is dominated by the in-plane motion.

In conclusion the method is clearly a sensitive indicator of a quantity related to s_d for the flames studied. The results show that more complex measurement set-ups may not result in significant extra information.

6 Effects of turbulent flow field on s_d^{2D}

It is expected that s_d^{2D} increases as the mixture is changed from lean to stoichiometric in analogy to how the laminar flame speed s_L behaves. Similarly one would expect an increase in s_d^{2D} with Re, as higher turbulence increases flame surface, stretch, and curvature, thus leading to higher reaction rates. Furthermore one would expect s_d^{2D} to be affected by acoustic forcing, as strong vortical motion affects flame stretch which includes curvature and strain effects. This thus offers potential to provide insight into mechanisms of thermoacoustic phenomena such as combustion instabilities. To elucidate these effects quantitatively, s_d^{2D} was investigated for various settings, including unforced and forced flames, different stoichiometries and Reynolds numbers.

The flame conditions investigated are listed in Table 1(a) to (h). Setting (b) is treated as the base case in the following, against which all other settings are compared. Flame (b) is operated at $\Phi = 0.550$, $Re = 17\,000$ and without acoustic forcing.

For settings (a) to (c), the Reynolds numbers (based on exit velocities) were increased from 14 000 to 22 000 whilst all other flame parameters remained unchanged. Settings (b), (d) and (e) were recorded at the same Re-number of 17 000, with no acoustic forcing present but at changing sto-
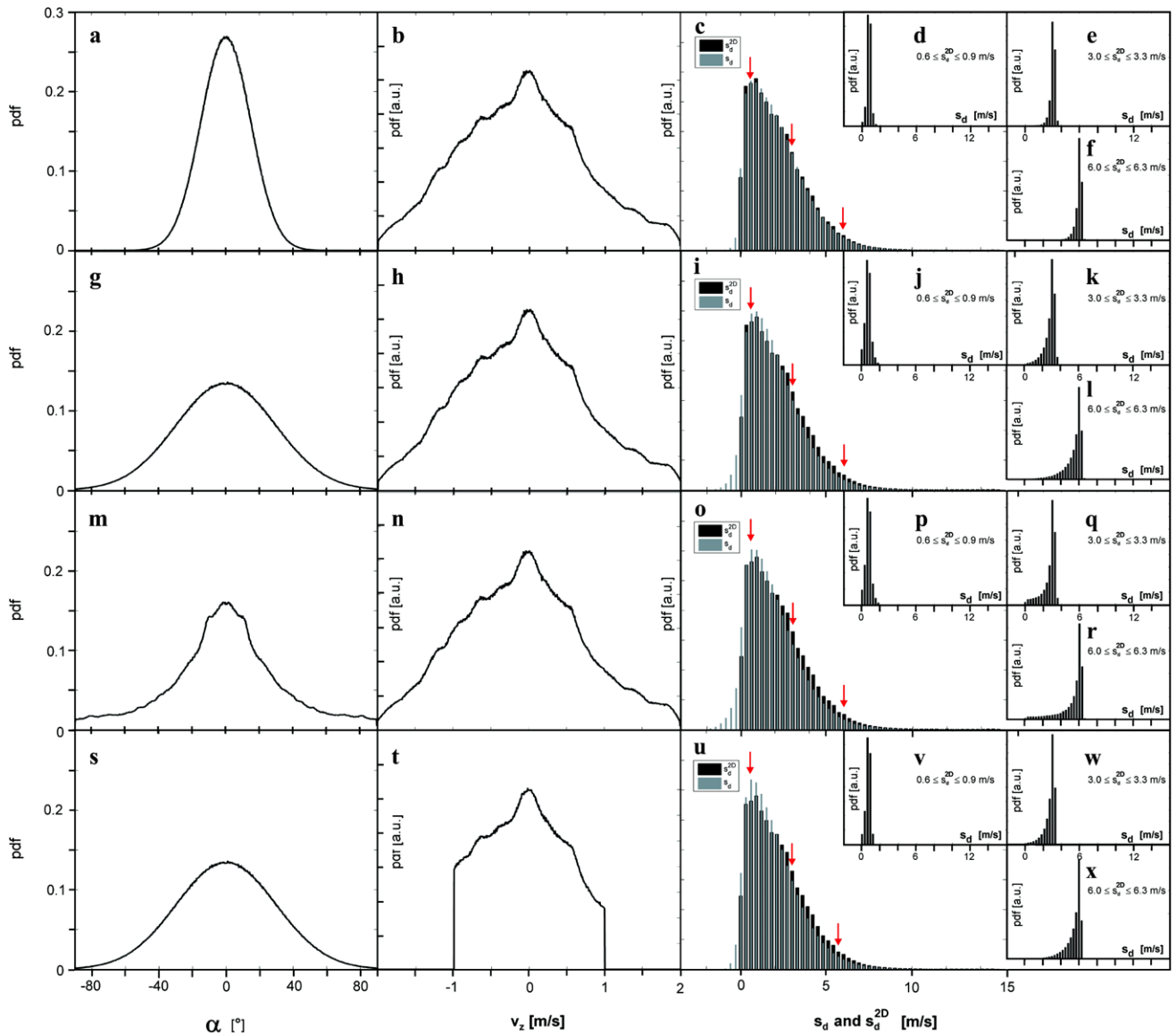
Fig. 11 Statistical comparison between s_d and s_d^{2D} based on assumed and measured angle distributions for α. pdfs for α are shown in the first column. The second column shows the measured pdf for v_z. The last column compares the pdfs for the measured s_d^{2D} with those for the true flame displacement speed s_d for different α distributions. Insets show the distributions of s_d for selected bins of s_d^{2D} (see main text for further explanations). Figures (**a**) to (**f**): assume the distribution of α to be Gaussian with {FWHM 35°}; Figures (**g**) to (**l**): assume the distribution of α to be Gaussian with {FWHM 70°}; Figures (**m**) to (**r**): assume the pdf of α to follow the same distribution as β (angle between flame dis-

placement speed vector and the normal of the mean-progress-variable, see main text); Figures (**s**) to (**x**): assume the distribution of α to be Gaussian with {FWHM 70°} and v_z of range -1 m/s $\leq v_z \leq +1$ m/s; (**a**), (**g**) and (**s**): pdfs of α and (**m**): pdf of β; (**b**), (**h**), (**n**) and (**t**): pdf of v_z; (**c**), (**i**), (**o**) and (**u**): pdf of s_d {calculated from Monte Carlo simulation} and s_d^{2D} {experiment}; (**d**), (**j**), (**p**) and (**v**): Conditioned pdf of s_d for $s_d^{2D} = 0.6$ to 0.9 m/s; (**e**), (**k**), (**q**) and (**w**): Conditioned pdf of s_d for $s_d^{2D} = 3.0$ to 3.3 m/s; (**f**), (**l**), (**r**) and (**x**): Conditioned pdf of s_d for $s_d^{2D} = 6.0$ to 6.3 m/s

ichiometry ($\Phi = 0.550$ to 0.700). Insight into the influence of forcing on the variation of s_d^{2D} is obtained by comparing flames (b), (f), (g) and (h), between which the only parameter varied is acoustic forcing amplitude. The forcing was increased gradually from the base case (b, no forcing), $u'/\bar{u} = 0.12$ (case f), $u'/\bar{u} = 0.32$ (case g) to $u'/\bar{u} = 0.65$ (case h). $u'/\bar{u}$ denotes the fluctuation over the mean inlet velocity.

The magnitude of the experimentally obtained values s_d^{2D} have to be corrected for the reduced gas density according to (3) at the location of the flamefront due to temperature elevation of gases in the reaction zone. These corrected values s_{d*}^{2D} can then be compared to the laminar burning velocity s_L. Since the gas density at the location of the flamefront was not measured, s_{d*}^{2D} was estimated as follows:

Table 1 Statistical analysis of s_d^{2D} for different flame settings: $\bar{s}_d^{2D}$ refers to the mean of the experimentally obtained s_d^{2D}; std($\bar{s}_d^{2D}$) denotes the one-sigma interval for the standard deviation of s_d^{2D}; $\bar{s}_{d*}^{2D}$ is the two-dimensional projection of the density-weighted flame displacement speed according to (10); s_L is the laminar burning velocity for C_2H_4/air [37]

Setting	a	b	c	d	e	f	g	h
Forcing amplitude (160 Hz, 20°; $u'/\bar{u}$)			–			0.12	0.32	0.65
Stoichiometry		0.550		0.625	0.700		0.550	
$\bar{u}$ [m/s]	8.1	9.9	12.7			9.9		
Re-number	14 000	17 000	22 000			17 000		
$\bar{s}_d^{2D}$ [m/s]	1.84	2.00	2.48	2.32	2.74	1.82	2.62	2.65
std($\bar{s}_d^{2D}$) [m/s]	1.39	1.62	2.22	1.55	2.12	1.56	2.89	2.91
Median($\bar{s}_d^{2D}$) [m/s]	1.73	1.73	1.93	1.93	2.45	1.37	1.83	1.93
$\rho_0/\rho \approx T_F/T_0$		4.6		4.8	5.1		4.6	
$\bar{s}_{d*}^{2D}$ [m/s]	0.40	0.43	0.54	0.48	0.54	0.40	0.57	0.58
s_L [m/s]	0.20	0.20	0.20	0.28	0.36	0.20	0.20	0.20
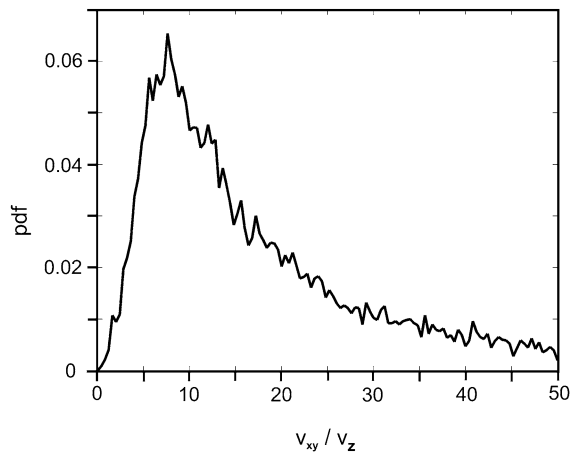
Fig. 12 Pdf of ratio v_{xy} to v_z for flame setting (b)

$$s_{d*}^{2D} = \frac{\rho}{\rho_0} s_d^{2D} \approx \frac{T_0}{T_F} \cdot s_d^{2D}, \qquad (10)$$

where T_F is the temperature at the position of the flame-front pixel-line, and T_0 the initial temperature of the reactant gas flow. T_F was not directly accessible from the experimental data set. Thus laminar premixed flame model calculations were conducted to obtain estimates for T_F. The PREMIX code [38] was used for burner stabilised one-dimensional flames with a known flux of reactants. For given stoichiometries, temperature and OH-radical concentration profiles were calculated. Recalling from Sect. 4.1, the flame-front was selected at the position of maximum gradient in the concentration contour of the OH-radical. Accordingly, temperatures calculated at these maximimum gradient isocontours were substituted for T_F in (10). The ratios T_F/T_0 were found to be 4.6, 4.8 and 5.1, respectively, for the investigated stoichiometries of 0.550, 0.625 and 0.700.

The investigation of Re-number effects on s_{d*}^{2D} (cases (a), (b) and (c)) show a clear correlation of s_{d*}^{2D} with increasing Re (Fig. 13(a)). The increasing turbulence causes increases in flame wrinkling and strain leading to an increase in stretch and reaction surface area. This is believed to be the main mechanism for the growth in s_{d*}^{2D} in our case. This observation is similar to what has been predicted theoretically [39]. The flame thickness was similar to, or smaller than, the scale of the smallest eddies in the flow field, and reaction surfaces appeared to remain connected and "flamelet" like throughout the explored parameter space. Finite-rate chemistry effects such as extinction were not evident for any Re numbers investigated. For very high turbulence levels, however, the growth of s_{d*}^{2D} with Re is expected to halt or even reverse [40], but this was not possible to explore under the current operating conditions.

s_{d*}^{2D} is clearly seen to increase as Φ is increased from 0.55 to 0.70 (cases (b), (d) and (e)) as seen on Fig. 13(b). The plot also shows the corresponding behaviour for s_L, which is well documented in the literature [37]. Comparing s_d and s_L, one sees that the two curves follow similar trends with Φ although there is a consistent offset of s_{d*}^{2D} to higher speeds (by around 0.2 m/s). Turbulence leads to wrinkling of the flamefront leading to an increase in flame surface area. This is associated with increased stretch and thus a steepening of reaction gradients. This in turn would increase the normal diffusion component to the flame displacement speed, s_{n*} (see (4) and (6)). Furthermore, in contrast to the one-dimensional laminar flame on which calculations of s_L are based, s_{t*} is no longer zero, as flamefront wrinkling (and curvature) causes appreciable tangential diffusion effects (see (4) and (7)).

The effect of acoustic forcing (cases (b), (f), (g) and (h)) on s_{d*}^{2D}, appears to increase s_{d*}^{2D} with forcing amplitude (Fig. 13(c)). There is a distinct increase in s_{d*}^{2D} from ca. 0.45 to around 0.6 m/s as $u'/\bar{u}$ changes from 0 to 0.65. A rationale for this strong dependence on forcing may be found on inspection of corresponding flame surface density data [41] for these conditions, which were calculated with a procedure as described in [23]. The flame surface density (FSD) is a statistical flame property used in the computational modelling of turbulent premixed flames as an estimate of reaction rate.
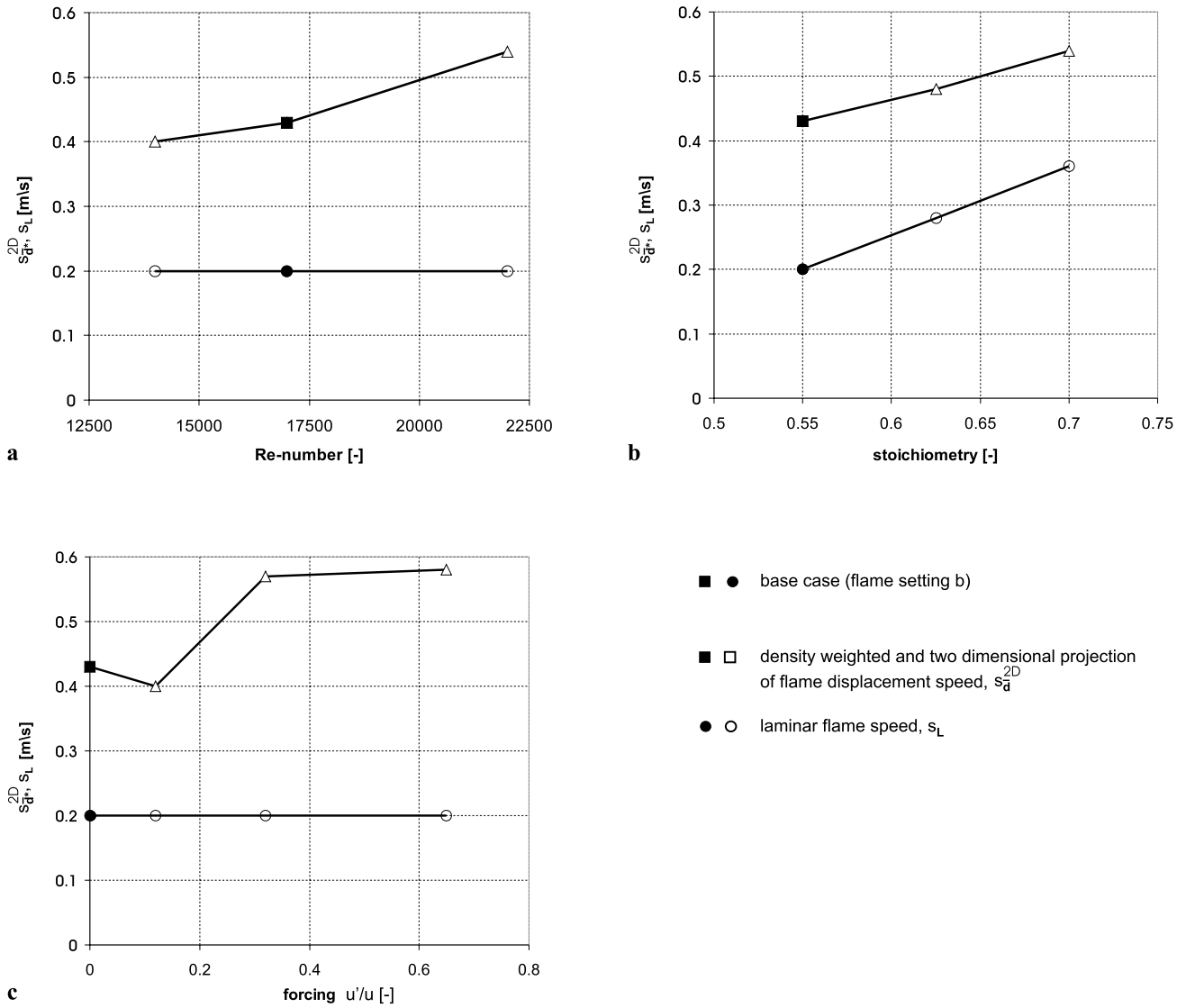
Fig. 13 Results on s_{d*}^{2D} for different flame settings: (**a**) $\bar{s}_{d*}^{2D}$ and s_L for cases (a), (b) and (c); (**b**) $\bar{s}_{d*}^{2D}$ and s_L for cases (b), (d) and (e); (**c**) $\bar{s}_{d*}^{2D}$ and s_L for cases (b), (f), (g) and (h)

FSD is given by the ratio of flame area divided by flame volume. Due to the two-dimensional character of the PLIF and SPIV measurements, FSD is calculated as flame length divided by flame area. FSD was calculated using a 5×5 pixel kernel over the instantaneous flame contour, where the magnitude of FSD at the central pixel of the kernel is given by

$$\text{FSD} = \frac{P_{nf}}{P_f} \cdot \frac{1}{R}, \tag{11}$$

where P_{nf} is the number of pixels which are *not* part of the flamefront, P_f the number of pixels *marking* the flamefront, and R the resolution. This procedure was carried out over the entire image (see Fig. 14). This was done for about 70 images, which were acquired under equivalent settings (sto-ichiometry, Re-number, forcing-amplitude and phase angle). This resulted in an averaged FSD-image per setting.

The results obtained are plotted in Fig. 15. Vortex shedding caused by the forcing results in dramatic contortions of the reaction surface, greatly increasing surface area, but also flame curvature, both of which would tend to increase s_{n*} and s_{t*}. In a previous publication [24, 42] we have evaluated flame transfer functions based on heat release rate measurements, and similar increases were observed. Similarly to what was found in these previous measurements, we also here see a "leveling off" at very high forcing amplitudes, which may be indicative of the onset of saturation behaviour in the flame's response, although further measurements are needed to validate this hypothesis.

Fig. 14 Determination of flame surface density (FSD). A interogation of 5×5 pixels is scanned of over the entire image, and the mean of the interrogation region is allocated to the centre pixel of the interrogation region as the value of FSD
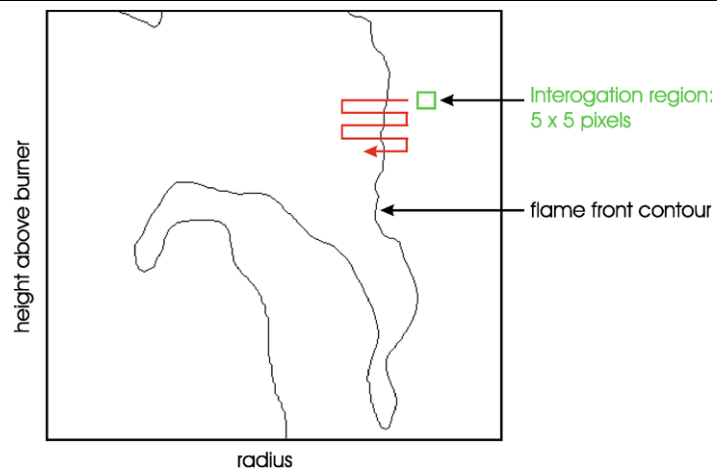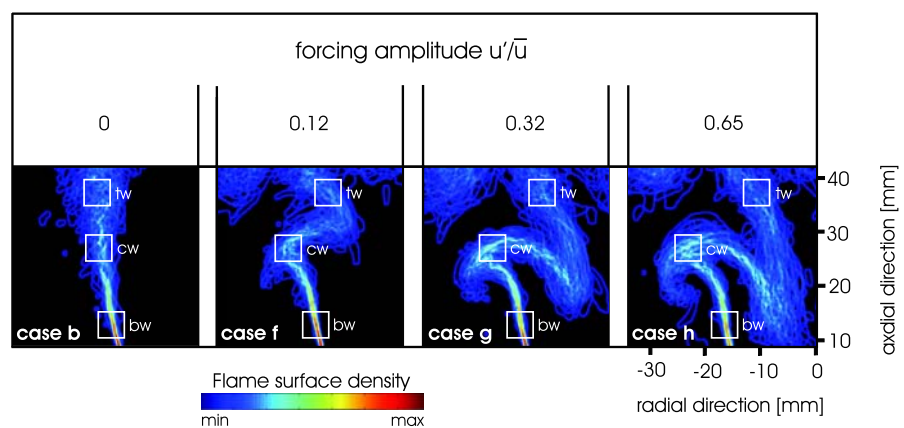

Fig. 15 Flame surface density for several forced flame settings: cases (b), (f), (g) and (h). The windows marked in the images are used for the description of Fig. 17: tw = top window; cw = central window and bw = bottom window. Scales as shown in Fig. 16

The flame surface density plots shown in Figs. 16 and 15 can be used to identify individual flame regions over which to perform statistical analysis. Pixels in the rectangles labelled tw (top window), cw (centre window) and bw (bottom window) were analysed with results plotted in Figs. 17(a) to (f). For the unforced flame, the density weighted flame displacement speed s_{d*}^{2D} is plotted against Re in (a). Clearly, s_{d*}^{2D} is lowest for region bw, close to the burner exit plane, and s_{d*}^{2D} shows the largest increase in tw. In bw, s_{d*}^{2D} is closest to the laminar flame speed s_L increasing strongly in the higher flame regions. An explanation may be found from a study of the gas phase velocities obtained from the PIV measurements. In Fig. 17(b) the rms velocity fluctuations are shown exhibiting a very similar correlation with Re as s_{d*}^{2D} in bw, fluctuations are smallest, with largest fluctuations found in tw, demonstrating the effect of turbulence on the magnitude of s_d. This strong correlation ($r = 0.94$) is evident from Fig. 17(c), where s_{d*}^{2D} is plotted against rms(v_{xy}). It is noteworthy that extrapolation of the fitted line results in a y-axis intercept of 0.19 m/s, which is in excellent agreement with the laminar flame velocity for the flame conditions studied (see Table 1). This provides further confidence in the measurement technique presented here and shows that over the

conditions studied, s_{d*}^{2D} does indeed vary linearly with turbulence level in these cases.

The same correlations are plotted for the forced flames in Figs. 17(d) to (f) as functions of forcing amplitude $u'/\bar{u}$. From the plots in (d) and (e) it is seen that variation with forcing are only minor in regions bw and tw, but very distinctly increasing in cw, located at the apex of the vortical structure of the flame. This remarkable increase points to a strong geometrical effects affecting s_n^* and s_t^* through increasing curvature and stretch. In this region rms velocity variations are a clearly highest (rms(v_{xy}) up to 7.5 m/s), and this in turn correlates strongly with s_{d*}^{2D} as evident from Fig. 17(f). Corresponding fluctuations of rms(v_{xy}) in regions bw and tw on the other hand are much smaller than in cw (by a factor of up to $\sim$7), and similar displacement speeds s_{d*}^{2D} are observed here, as in the corresponding unforced flame. Note that again in the limit of the rms $v_{xy} = 0$ one obtains a value of $\bar{s}_{d*}^{2D} = 0.21$ m/s at the intercept with the y-axis, again in excellent agreement with v_L for these conditions. These findings suggest that, for the conditions studied, rms v_{xy} is an appropriate and sufficient parameter to quantify s_{d*}^{2D} for the range of conditions studied in this work. Current efforts are aimed at investigating correlations

Fig. 16 Flame surface density for several unforced flame settings: cases (a), (b), (c), (d) and (e). The windows marked in the images are used for the description of Fig. 17: tw = top window; cw = central window and bw = bottom window
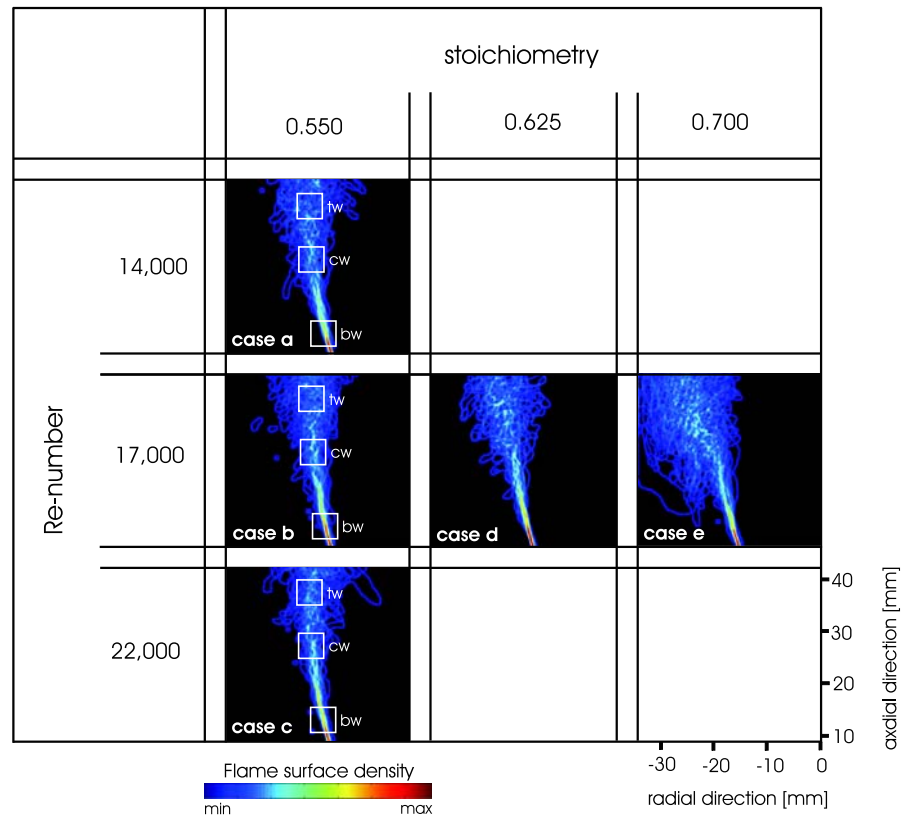
with flame strain, curvature and stretch, which, based on the current findings, we would expect to correlate in similar fashion with rms v_{xy}. In a recent publication [43] the influences of flamefront curvature and strain rates are evaluated for methan–air and hydrogen–air flames.

7 Summary and conclusion

In this paper, a novel approach to measure the density weighted local flame displacement speed s_{d*}^{2D} in turbulent lean premixed flames is presented. s_{d*}^{2D} is a useful quantity for comparison with CFD and can also be compared directly to the laminar flame speed s_L calculated for the same stoichiometries. The method is based on the simultaneous application of time-sequenced planar laser-induced fluorescence and stereoscopic particle image velocimetry. In combination, these permit us to isolate convective, chemical and geometrical effects on the local flamefront propagation and correlate these to flow parameters such as turbulence intensity, or in the case of acoustic forcing, to amplitude variations on imposed flow fluctuations. The method effectively retraces the "time history" of the flow field and uses this information to differentiate between the convective and chemical phenomena occurring in the flame. This permits a new method for quantification of turbulence/chemistry interactions with interesting potential for CFD validation and calibration. An

important result coming out of this work is that the rms velocity fluctuation in the turbulent velocity field, rms(v_{xy}), local to the flamefront, appears to be a sufficient parameter to quantify s_{d*}^{2D}.

Increasing turbulence was observed to result in an increasing density-weighted flame displacement speed. Flame surface density data showed strong flame wrinkling and thus stretching of the flame surface in highly turbulent regions. This in turn leads to a thinning of the flame brush and increase of the tangential and normal components of the flame displacement speed. For an *increasing stoichiometry*, it was observed that the density-weighted flame displacement speed s_{d*}^{2D} shows values which are higher by a nearly constant offset of 0.2 m/s than the laminar flame speed s_L. A flame subjected to *acoustic forcing* shows a strong increase of s_{d*}^{2D} with increased acoustic forcing. As illustrated by the flame surface density plots, an increase of the forcing amplitude is accompanied by a strong growth of flame surface area, and flame stretch possibly linked to increases in the tangential and normal components of the flame displacement speed. A saturation of this trend appears to occur at half-maximum forcing amplitudes ($u'/\bar{u} = 0.32$), which agrees with similar trends observed in previous measurements of flame-transfer-functions for this flame. Final conclusions on saturation effects do however still require further analysis.
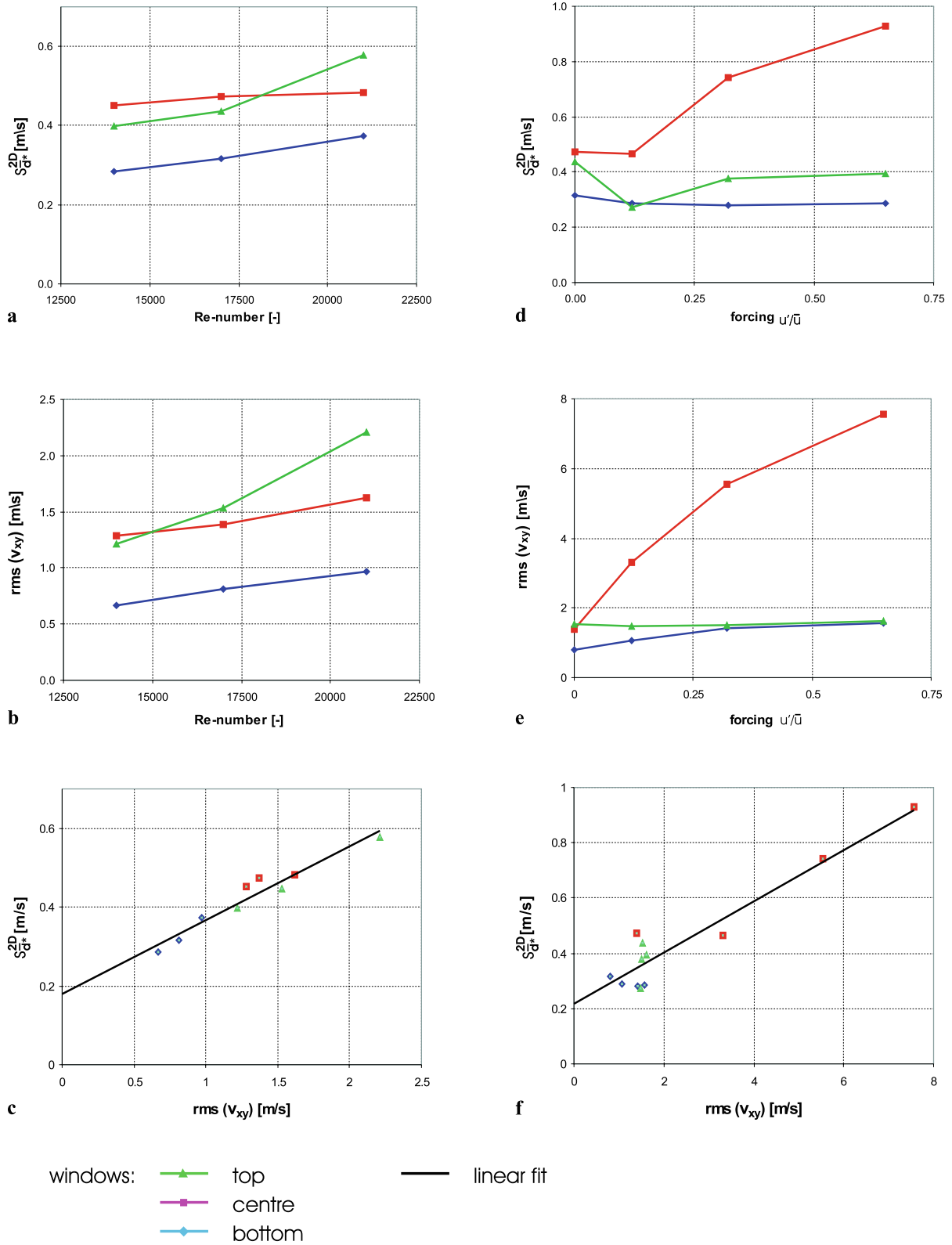
Fig. 17 Experimentally obtained and density weighted mean values of s_{d*}^{2D} for different windows (see Figs. 16 and 15) within the field of view: (**a**) plots (**a**), (**b**) and (**c**): investigation of unforced flame settings for increasing *Re*-number (flame settings (a), (b) and (c)). (**b**) plots (**d**), (**e**) and (**f**): investigation on the magnitude of forcing—flame settings (flame settings (b), (f), (g) and (h))

References

1. M. Klein, N. Chakraborty, K.W. Jenkins, R.S. Cant, Experimental investigation of three-dimensional flame-front structure in premixed turbulent combustion—II. Lean hydrogen/air Bunsen flames. Phys. Fluids **18**(055102), 1–15 (2006)

2. N. Swaminathan, R.W. Bilger, G.R. Ruetsch, Interdependence of the instantaneous flame front structure and the overall scalar flux in turbulent premixed flames. Combust. Sci. Technol. **128**, 73–97 (1997)

3. A. Lipatnikov, J. Chomiak, A theoretical study of premixed turbulent flame development. Combust. Inst. **30**, 843–850 (2005)

4. J. Fielding, M.B. Long, G. Fielding, M. Komiyama, Systematic errors in optical-flow velocimetry for turbulent flows and flames. Appl. Opt. **40** (2000)

5. S. Gashi, J. Hult, K.W. Jenkins, N. Chakraborty, R.S. Cant, C. Kaminski, Curvature and wrinkling of premixed flame kernels—comparison of OH-PLIF and DNS data. Proc. Combust. Inst. **30**, 809–817 (2005)

6. J. Hult, M. Richter, J. Nygren, M. Aldén, A. Hultqvist, M. Christensen, B. Johansson, Application of a high-repetition-rate laser diagnostic system for single-cycle-resolved imaging in internal combustion engines. Appl. Opt. **41**(24), 5002–5014 (2002)

7. T.W. Lee, S.J. Lee, Direct comparison of turbulent burning velocity and flame surface properties in turbulent premixed flames. Combust. Flame **132**, 492–502 (2003)

8. E. Conte, K. Boulouchos, Experimental investigation into the effect of reformer gas addition on flame speed and flame front propagation in premixed, homogeneous charge gasoline engines. Combust. Flame **146**, 329–347 (2006)

9. Y.C. Chen, R.W. Bilger, Experimental investigation of three-dimensional flame-front structure in premixed turbulent combustion—II. Lean hydrogen/air Bunsen flames. Combust. Flame **138**, 155–174 (2004)

10. R. Abu-Gharbieh, G. Hamarneh, T. Gustavsson, C.F. Kaminski, Level set curve matching and particle image velocimetry for resolving chemistry and turbulence interactions in propagating flames. J. Math. Imaging Vis. **19**, 199–218 (2003)

11. C.F. Kaminski, X.S. Bai, J. Hult, A. Dreizler, S. Lindenmaier, L. Fuchs, Flame growth and wrinkling in a turbulent flow. Appl. Phys. B, Lasers Opt. **71**, 711–716 (2000)

12. J. Hult, U. Meier, W. Meier, A. Harvey, C.F. Kaminski, Experimental analysis of local flame extinction in a turbulent jet diffusion flame by high repetition 2D laser techniques and multi-scalar measurements. Proc. Combust. Inst. **30**, 701–709 (2005)

13. C.F. Kaminski, J. Hult, M. Alden, High repetition rate planar laser induced fluorescence of OH in a turbulent non-premixed flame. Appl. Phys. B, Lasers Opt. **68**, 757–760 (1999)

14. T. Echekki, J.H. Chen, Unsteady strain rate and curvature effects in turbulent premixed methane-air flames. Combust. Flame **116**, 184–202 (1996)

15. N. Chakraborty, E. Mastorakos, Numerical investigation of edge flame propagation characteristics in turbulent mixing layers. Phys. Fluids **18**(105103), 513–523 (2006)

16. N. Chakraborty, R.S. Cant, Influence of Lewis number on strain rate effects in turbulent premixed flame propagation. Heat Mass Transf. **49**, 2158–2172 (2006)

17. C. Pantano, Direct simulations of non-premixed flame extinction in a methane-air jet with reduced chemistry. J. Fluid Mech. **541**, 231–270 (2004)

18. C. Yoo, H.G. Im, Transient dynamics of edge flames in a laminar nonpremixed hydrogen-air counterflow. Proc. Combust. Inst. **30**, 349–356 (2004)

19. N. Peters, P. Terhoeven, J.H. Chen, T. Echekki, Statistics of flame displacement speeds from computations of 2D methane-air flames. Proc. Combust. Inst. **27**, 833–840 (1998)

20. N. Chakraborty, R.S. Cant, Unsteady effects of strain rate and curvature on turbulent premixed flames in inlet-outlet configuration. Combust. Flame **137**, 129–147 (2004)

21. N. Peters, *Turbulent Combustion* (Cambridge University Press, Cambridge, 2000)

22. B. Ayoola, G. Hartung, C.A. Armitage, J. Hult, R.S. Cant, C.F. Kaminski, Temperature response of turbulent premixed flames to inlet velocity oscillations. Exp. Fluids **46**, 27–41 (2009)

23. R. Balachandran, B.O. Ayoola, C.F. Kaminski, A.P. Dowling, E. Mastorakos, Experimental investigation of the nonlinear response of turbulent premixed flames to imposed inlet velocity oscillations. Combust. Flame **143**(1–2), 37–55 (2005)

24. R. Balachandran, Experimental investigation of the response of turbulent premixed flames to acoustic oscillations, Ph.D. thesis, University of Cambridge, Department of Engineering, Cambridge, UK, 2006

25. B.O. Ayoola, R. Balachandran, J.H. Frank, E. Mastorakos, C.F. Kaminski, Spatially resolved heat release rate measurements in turbulent premixed flames. Combust. Flame **144**(1–2), 1–16 (2006)

26. G. Hartung, J. Hult, C.F. Kaminski, J. Rogerson, N. Swaminathan, Effect of heat release on turbulence and its interaction with scalar in premixed combustion. Phys. Fluids **20**, 445–473 (2008)

27. F. Scarano, M.L. Riethmuller, Iterative multigrid approach in PIV image processing with discrete window offset. Exp. Fluids **26**(12), 513–523 (1999)

28. H. Malm, G. Sparr, J. Hult, C.F. Kaminski, Nonlinear diffusion filtering of images obtained by planar laser-induced fluorescence spectroscopy. J. Opt. Soc. Am. A **17**(12), 2148–2156 (2000)

29. J. Canny, A computational approach to edge-detection. IEEE Trans. Pattern Anal. Mach. Intell. **8**(6), 679–698 (1986)

30. IDL, IDL—technical programming language. http://www.ittvis.com/idl/, 2007

31. K. Jambunathan, X.Y. Ju, B.N. Dobbins, S. Ashforthfrost, An improved cross-correlation technique for particle image velocimetry. Meas. Sci. Technol. **6**(5), 507–514 (1995)

32. I. Boxx, C. Kittler, R. Gordon, B. Böhm, M. Aigner, A. Dreizler, W. Meier, Simultaneous three component PIV/OH-PLIF measurements of a turbulent lifted, C_3H_8-argon jet diffusion flame at 1.5 kHz repetition rate. Proc. Combust. Inst. **32**(1), 905–912 (2009)

33. A.M. Steinberg, J.F. Driscoll, S.L. Ceccio, Measurements of turbulent premixed flame dynamics using cinema stereoscopic PIV. Exp. Fluids **44**, 985–999 (2008)

34. R. Chrystie, I.S. Burns, J. Hult, C. Kaminski, On the improvement of two-dimensional curvature computation and its application to turbulent premixed flame correlations. Meas. Sci. Technol. **19**, 125503 (2008)

35. J. Rehm, N. Clemens, The association of scalar dissipation rate layers and the OH zones with strain, vorticity, and 2D dilitation fields in turbulent nonpremixed jets and jet flames, American Institute of Aeronautics and Astronautics, Reston, VA. Paper No. AIAA-99-0676, 1999

36. Y.-C. Chen, R.W. Bilger, Experimental investigation of three-dimensional flame front structure in premixed turbulent combustion—I: hydrocarbon/air Bunsen flames. Combust. Flame **131**(4), 400–435 (2002)

37. T. Hirasawa, C.J. Sung, A. Joshi, Z. Yang, H. Wang, C.K. Law, Determination of laminar flame speeds using digital particle image velocimetry: binary fuel blends of ethylene, n-butane, and toluene. Proc. Combust. Inst. **29**, 1427–1434 (2002)

38. R.J. Kee, J.F. Grcar, M.D. Smooke, J.A. Miller, A FORTRAN program for modelling steady laminar one-dimensional premixed flames. Sandia National Laboratories Report SAND85-8240, 1993

39. P. Flohr, H. Pitsch, A turbulent flame speed closure model for LES of industrial burner flows, Centre of Turbulence Research, Proceedings of the summer programme, University of Stanford, Stanford, USA, 2000, pp. 169–179

40. V.L. Zimont, A.N. Lipatnikov, A numerical model of premixed turbulent combustion of gases. Chem. Phys. Rep. **14**(7), 993–1025 (1995)

41. J. Hult, S. Gashi, N. Chakraborty, M. Klein, K.W. Jenkins, S. Cant, C.F. Kaminski, Measurement of flame surface density for turbulent premixed flames using PLIF and DNS. Combust. Inst. **31**, 1319–1326 (2007)

42. B. Ayoola, Laser-based measurement of heat release rate and temperature in turbulent premixed flames, Ph.D. thesis, University of Cambridge, Department of Chemical Engineering, Cambridge, UK, 2006

43. J.H.C.N. Chakraborty, E.R. Hawkes, R.S. Cant, Effects of strain rate and curvature on surface density function transport in turbulent premixed CH_4-air and H_2-air flames: A comparative study. Combust. Flame **154**, 259–280 (2008)